Permeability of Monodisperse Solid Foams

Olivier Pitois, Asmaa Kaddami, Vincent Langlois

Permeability of monodisperse solid foams

Olivier Pitois*, Asmaa Kaddami and Vincent Langlois

Lab Navier, Univ Gustave Eiffel, ENPC, CNRS, F-77447 Marne-la-Vallée, France.

* corresponding author: olivier.pitois@ifsttar.fr

Abstract:

Fluid permeability of solid foams is a crucial parameter to control transport phenomena in numerous engineering applications, such as heat exchangers or filters for example. Open-cell foams with monodisperse pore diameter ranging from 200 to 1000 µm and solid volume fraction ranging from 0.1 to 0.38 are produced and Darcy permeability is measured. The permeability divided by the square of the pore size shows an exponential decay as a function of solid volume fraction. Surprisingly, existing models do not capture this exponential decay and actually they predict permeability values significantly larger than the measured values. The observed exponential decay is then successfully described by using models based on the viscous dissipation occurring through the apertures that connect the foam pores and by accounting for both the mean size of the apertures and the mean number of apertures per pore.

Highlights

- Monodisperse solid foams have been produced with both controlled pore size and void fraction
- The dimensionless permeability is shown to decrease exponentially over the full range of void fractions
- The exponential behavior is successfully modelled from both the viscous dissipation occurring through pore connections and the mean number of apertures per pore

1. Introduction

Open cell solid foams are attractive materials used in various industries, especially as heat exchangers [1] or as thermal insulation materials [2], as crash energy [3] or acoustical absorbers [4], as filters for fluids, ... For many of those applications, permeability is a crucial parameter: as examples, it sets the pressure required to filter a given volume flow rate of fluid, and it is used to model sound absorption through foams [5].

In spite of the significant amount of work devoted to study foam permeability (see [6,7] for recent reviews), strong discrepancies appears within the literature results. The main reasons for such discrepancies seem to be related to measurement and data treatment issues, to the use of different morphological definitions (number of pores per inch, strut width, strut length, aperture diameter, pore diameter, …), to the large spectrum of different materials called *foams* (replication or capillary foams, fully open or partially open cells, …), to the limited range of void fraction available for each studied foam, …

Actually, there is no general consensus to define the link between permeability and foam microstructure, and this limits the development of general models [6]. In order to increase our understanding about foam permeability, we perform experiments with monodisperse foams which were produced on purpose with several pore sizes and within a large range of void fraction. As shown in the following, monodispersity is very helpful for careful comparisons to be made with existing models, which will allow highlighting the ability of the so-called *aperture model* to describe our set of permeability values.

2. Production and characterization of the solid foam samples

Studied solid foams are geopolymer foams produced from metakaolin (MK) particles by using a dedicated process presented in the following.

2.1. Materials

We used an activating solution prepared by mixing NaOH solution (mass concentration C_w = 0.35) with a solution containing Na_2O (C_w = 0.08) and SiO_2 (C_w = 0.27) provided by MERCK KGaA, and water. The density is ρ_ℓ = 1400 kg/m^3 and the chemical composition is given by molar ratios H_2O/Na_2O = 14.68 and SiO_2/Na_2O = 1.01.

Metakaolin (MK) particles were provided by AGS Minéraux (France): Argical M 1200s. Chemical compositions: SiO_2 55.0%, Al_2O_3 39.0%, Fe_2O_3 1.8%, TiO_2 1.5%, K_2O+Na_2O 1.0%, CaO+MgO 0.6%. As provided by the supplier: BET specific surface area is equal to 19 m^2/g and median diameter of the volume weighted size distribution is approximately $d_p \approx$ 2 µm. Their density is ρ_{MK} = 2200 kg/m^3.

The activated MK suspensions were prepared by mixing a mass m_ℓ of the activating solution with a mass m_{MK} of metakaolin particles. The suspension is characterized by the ratio $L/S =$

m_ℓ/m_{MK}. For the present study L/S was within the range 1.75-2. The chemical composition of those samples is given by Si/Al and Na_2O/Al_2O_3 ratios, respectively within the ranges 1.8-2.5 and 1.2-2.7. The typical setting time is about two hours.

Glucopon® 225 DK (alkyl polyglycoside provided by BASF) was used as surfactant for foaming purpose. Such a nonionic surfactant of molar mass equal to 420 g/mol was shown to be suitable to stabilize the foam morphology during the two hours preceding the geopolymerization stage. Surface tension of Glucopon water solutions was measured to be σ = 30 mN/m for concentrations above the critical micellar concentration. Dynamic viscosity of such water solutions is very close to that of pure water, i.e. 10^{-3} Pa.s.

2.2. Production

The method used for the production of controlled MK foams has been presented in a previous paper [8]. Here we recall the main steps but the reader can refer to [8] for more details.

In broad outline, metakaolin foams are produced by mixing precursor aqueous foam with the metakaolin (MK) suspension described previously. The production process consists of two steps: (1) production of the precursor aqueous foam, (2) mixing of the precursor aqueous foam with the MK suspension and in-line filling of the resulting MK fresh foam in a vessel.

Step 1: Aqueous foam is generated by pushing both gas (nitrogen) and foaming liquid (glucopon water solution) through a T-junction. Tuning the gas/liquid flow rates ratio allows producing monodisperse bubbles with chosen diameters ranging between 200 µm and few millimeters. Generated bubbles are continuously collected into a vertical glass column. The average bubble diameter D_b is measured using a camera focused at the wall of the column in order to control this parameter. For foam made with bubble size $D_b \gtrsim$ 500 µm, ripening turns out to be insignificant over the duration of the production step, so highly monodisperse precursor aqueous foams were obtained. In contrast, smaller bubble sizes were observed to evolve during the production step because of the ripening process. This can be explained by both the increase of the ripening rate for smaller bubbles (see page 104 of [9]) and the decrease of the production rate (larger time required to produce the same volume of foam) for smaller bubbles. Such an evolution was efficiently counteracted by using perfluorohexane as a saturating vapor in the bubbling gas [10].

Step 2: After production of the required precursor foam volume, the latter is pushed with the MK suspension through a static mixer (flow focusing device and classical helical geometries). The gas

volume fraction within the resulting MK foam can be adjusted by tuning the ratio of flow rates for the precursor foam and the MK suspension. The resulting fresh foam is continuously pushed in a sample vessel of diameter 26 mm and height H_0 = 50 mm. Typical volume flow rates for the production of the studied samples are of the order of 10 mL/min. The vessel is filled to the top and closed. Note that the values for the solid volume fraction ϕ_s was also determined a posteriori by comparing the measured density of the fresh MK foam with the density of the MK suspension. After 2 days in the closed vessels, samples are let for drying at room temperature for 2 days before unmolding.

2.3. Foam microstructure

Optical microscopy was used to characterize the foam structure. Pore sizes were measured directly on pictures like Fig. 1b. According to our production method, the pore size in the solid foam is set by the initial bubble size in the liquid precursor foam. In other words, all the solid foams (a series) produced with the same precursor foam have the same pore size. It is to say that when measuring the pore size of such a series, it is preferable to turn to samples with higher ϕ_s because pores are more spherical and their diameter can be measured more conveniently. For each of those samples, twenty circular pore diameters were measured and the average value D_p was calculated. The expected error bar is $\Delta D_p/D_p \approx 5\%$. Apertures were measured as follows: twenty diameters of apertures that could be fitted with a circle (i.e. located within a plane perpendicular to the observation axis) were measured and the average value d_0 was calculated. The expected error bar is $\Delta d_0/d_0 \approx 5\%$.

In addition, X-ray tomography (EasyTom RX Solutions) were performed on few samples to obtain size distributions. Images of small samples (i.e. 5x5x10 mm) were obtained with a Ultratom scanner from RX solutions. Measurement involved a Hamamatsu L10801 X-ray source (160 kV) and a Paxscan Varian 2520 V at-panel imager. All scans were performed at 60 kV and 85 µA. Frame rate was 3 images per second and 12 images were averaged to produce one projection (the resulting effective exposure time is therefore 4s). 3D tomographic reconstruction was performed with the X-Act commercial software developed by RX-Solutions. Voxel size for the obtained images is 5 µm. Pores appear black on the reconstructed images and interstitial geopolymer solid is light grey. This allowed us to analyze the images with the freeware ImageJ program [11] to compute the pore size distribution: First, a closing filter from MorphoLibJ plugin [12] with a 2 voxel-radius ball element was applied to reduce noise from the images. Then, image threshold was calculated using the Otsu method [13]. 3D Watershed from MorphoLibJ was applied, then 1-voxel dilatation filter. Finally, 3D

Object Counter plugin returned the volume ($V_{p,i}$) of each pore, from which the equivalent pore diameter $D_{p,i} = \left(6V_{p,i}/\pi\right)^{1/3}$ was calculated, as well as the number average value. The averaged values determined following this method were found to be consistent with diameters measured by optical microscopy, i.e. the observed deviation is smaller than 5%. Apertures were identified as follows: the described-above binarized image was subtracted to the image resulting from the Watershed plugin, which materializes the apertures as thin planar objects on which the 3D Object Counter was used to get their sizes and positions. It appeared that the resulting mean aperture diameter was systematically smaller (by 25 µm) than the mean size measured by optical microscopy. In the following, aperture sizes d_o correspond to optical microscopy measurements, except for Fig. 1d that shows size distributions where the value obtained by X-ray tomography is corrected by -25 µm. The number of apertures per pore N_o was deduced by matching both pores and apertures positions. This was performed for each neighbor pore couple, for example a pore of diameter $D_{p,A}$ with center at position A and another of diameter $D_{p,B}$ at B, by seeking for an aperture object near its expected position P, defined by the average position along the axis passing through both pore centers and weighted by the pore sizes, i.e. $\overrightarrow{AP} = \frac{D_{p,A}}{D_{p,A}+D_{p,B}}\overrightarrow{AB}$.

2.4. Permeability measurement

Gas-flow permeability was measured with a home-made setup. A gas flow controller was used to push dry nitrogen at mass flow rate η within the range 0-10^{-5} kg/s (or equivalently a volume flow rate Q within the range 0-8 mL/s at P_0 = 10^5 Pa) through the foam sample (length L, typically within the range 3-5 cm, and circular cross-section S = 5.3 cm^2) embedded with PTFE ribbon and fitting a cylindrical tube. The pressure difference ΔP across the sample was measured thanks to a manometer with precision equal to 0.1 Pa and pressure range 0-250 Pa.

The flow of gas through solid foams can be described by the following equation [14]: $\rho\, dP/dL = -\eta(\mu/k_D + \beta\eta)$, where ρ is the gas density, μ = 1.758 10^{-5} Pa.s is the dynamic viscosity of the gas, k_D is the intrinsic foam permeability and β is the inertia factor. By assuming a perfect gas behavior we have $\Delta\rho/\rho_0 = \Delta P/P_0$, with P_0 = 10^5 Pa and ρ_0 = 1.25 kg/m^3. Here we consider the maximum pressure drop value in our experiments, i.e. $\Delta P_{max} \approx 250$ Pa, which means that $(\Delta\rho/\rho_0)_{max} \approx 0.25\%$. This shows that gas compressibility can be reasonably neglected in our experiment. Moreover, by using values we obtained for k_D (see Table 1), the ratio $\beta\eta k_D/\mu$ is calculated to be of the order of 0.1% (we used [14]: $\beta = 0.84/D_p$), which means that the above equation boils down to the Darcy law: $dP/dL = -(Q/S)\mu/k_D$. When considering inertia effects, it

is usual to refer to the Reynolds number, $Re = \rho(Q/S)D_p/\mu$. Here we calculate the average value $\overline{Re}$ for each sample within our experimental conditions. It is shown in Table 1 that $0.1 \leq \overline{Re} \leq 0.6$, which suggests low inertia effects. Reported values for k_D were obtained by assuming the Darcy law and were determined as follows: $\Delta P/L$ values were plotted as a function of Q/S and the slope k_D/μ was determined by linear regression (see Fig. 3a). Note that all the measurements exhibit a linear behavior (see coefficients of determination $R^2 \approx 1$ in Table 1), which is consistent with the analysis presented above for inertia effects.

3. Results and discussion

First of all we describe the microstructure of our samples (see Fig. 1). Highly monodisperse open cell foams are obtained with several pores sizes. The effect of solid volume fraction is shown in Fig. 1b: foam can be described as interconnected struts at small ϕ_s values, but spherical pores with small circular apertures are seen for larger ϕ_s values. Sizes of the apertures appear to be more dispersed than pore sizes (see Fig. 1c & d), and their mean value decreases as a function of solid volume fraction. The number of apertures per pore N_o is shown in Fig. 1e for several samples. N_o decreases as a function of solid volume fraction: $N_o \cong 10$ for $\phi_s \cong 0.2$ and $N_o \cong 7$ for $\phi_s \cong 0.3$.

All our results for the mean aperture diameter d_o are presented in Fig. 2, showing the dimensionless parameter d_o/D_p as a function of ϕ_s. Aperture size decreases from $d_o/D_p \approx 0.4$ for $\phi_s \approx 0.05$ down to $d_o/D_p < 0.2$ for $\phi_s > 0.3$. Note that we don't report d_o values for $\phi_s > \phi_s^* \cong 0.38$ because apertures are scarce for such samples and the sample's homogeneity was not ensured. Actually the decrease of apertures size is very strong between 0.35 and ϕ_s^*, where it is expected to vanish. This behavior can be inferred from the known packing volume fraction of monodisperse spheres, for which the corresponding critical value is equal to 0.36. Besides, note that the aperture size measured at $\phi_s \approx 0.02$ for monodisperse open-cell polymer foams [4] shows good agreement with our data. Theoretical curves corresponding to ideal crystalline foam structures were obtained by numerical simulations (fine convergence was obtained by using the Surface Evolver – Fluid Interface Tool) and are plotted in Fig. 2. It appears that crystalline structures can be used to describe aperture values only within a small range of ϕ_s values, i.e. $\phi_s \lesssim 0.1$ for FCC (Face-Centered Cubic) and $0.1 \lesssim \phi_s \lesssim 0.2$ for BCC (Body-Centered Cubic). Actually, deviations are significant as ϕ_s gets close to the corresponding critical value, i.e. $\phi_s^* = 0.26$ for FCC and $\phi_s^* = 0.32$ for BCC. In capillary

foams the apertures diameter decreases abruptly as ϕ_s gets close to ϕ_s^* and it vanishes at ϕ_s^*. This evolution is expected to be described by a power law behavior [15], such as:

$$\frac{d_o}{D_p} \cong a(\phi_s^* - \phi_s)^b \qquad \text{(eq. 1)}$$

Fig. 2 shows that, close to $\phi_s \approx \phi_s^*$, each one of the three foam structures can be described by eq. 1 using the same values for a = 0.66 and b = 0.5.

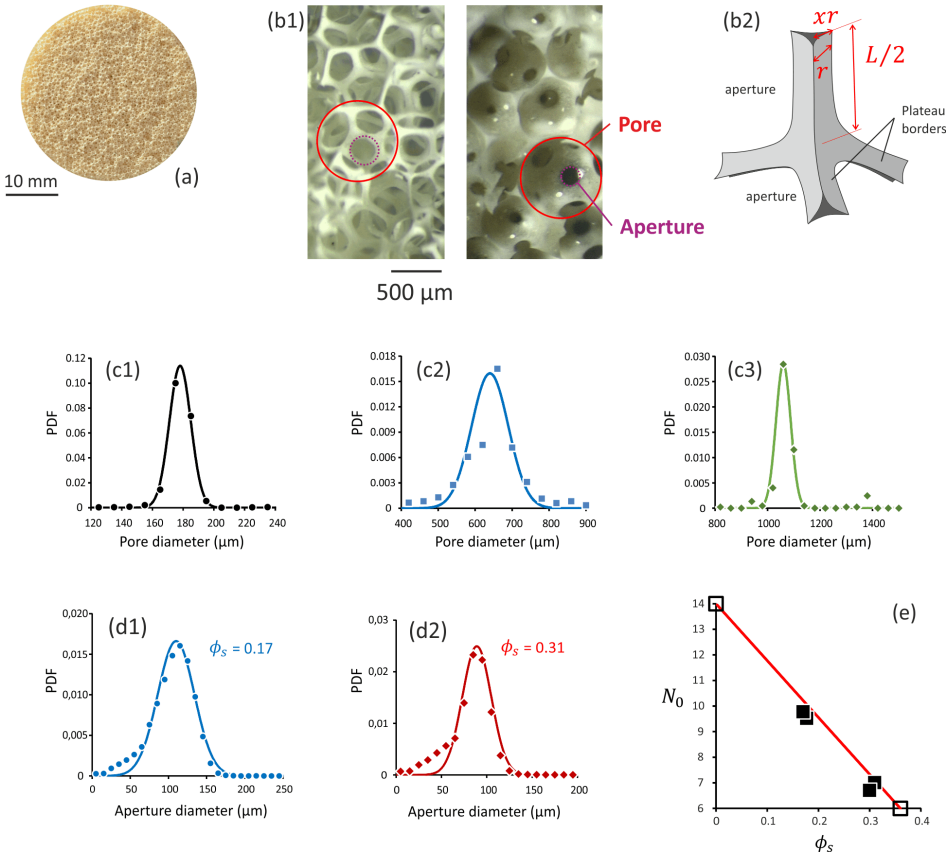

Figure 1: Microstructure of the solid MK foams. (a) Picture of a sample seen from above ($D_p \approx 600$ µm, ϕ_s = 0.2). (b1) Close-up of foam samples revealing the open-cell microstructure and showing pores (continuous lines) and pore apertures (dotted lines). Left: $D_p \approx 800$ µm, ϕ_s = 0.08; right: $D_p \approx 800$ µm, ϕ_s = 0.3. (b2) Scheme of the foam structure showing the Plateau border network and the apertures, which are the passages between the pores: L is the node-to-node distance, r is the thickness of the Plateau borders and xr corresponds to the covering length of the Plateau borders over apertures. (c) Number pore diameter (D_p) distribution (probability density function) for three samples. The three Gaussian curves are plotted with mean and standard deviation equal to: (C1) 188 µm and 7 µm, (C2) 640 µm and 50 µm, 1060 µm and 28 µm. (d) Number aperture diameter (d_o) distribution (probability density function) for two samples with same pore size $D_p \approx 300$ µm. The

Gaussian curves are plotted with mean and standard deviation equal to: (D1) 89 µm and 16 µm (sample ϕ_s = 0.31), 110 µm and 24 µm (sample ϕ_s = 0.17). (e) Mean number of apertures per pore as a function of solid volume fraction. Filled symbols: experimental data (five samples with size $D_p \approx$ 200, 300 and 600 µm). Empty symbols: theoretical values. The solid line corresponds to equation 11.

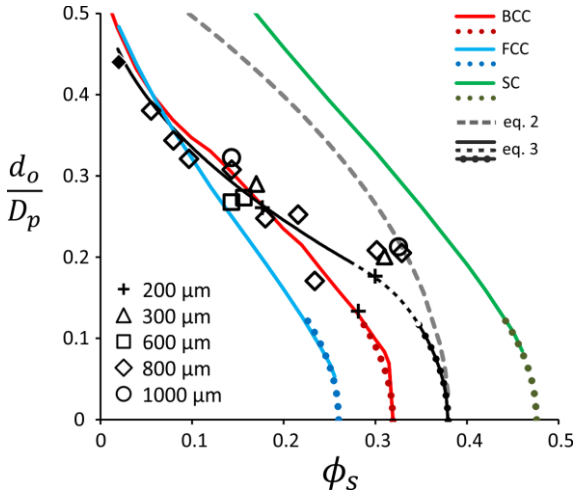

Figure 2: Diameter of apertures d_o divided by the pore diameter D_p as a function of solid volume fraction ϕ_s. Continuous curves show the theoretical values for several structures: red – Kelvin/BCC, blue – FCC, green – Simple Cubic. Note that both square and hexagonal faces are found in the Kelvin structure, so an area-weighted average value is presented. Dotted curves correspond to power law functions: $d_o/D_p = 0.66(\phi_s^* - \phi_s)^{0.5}$ with ϕ_s^* equal to 0.32 for BCC (red), 0.26 for FCC (blue), 0.476 for CC (green) and 0.38 for the black dots. The dashed line corresponds to eq. 2 [16]*. Continuous, dashed and dotted black lines correspond to eq. 3. Empty symbols: experimental data for MK foam samples with different pore sizes and different solid volume fractions. Filled symbol: data published by Trinh et al.*[4] *for monodisperse open-cell polymer foams.*

The description of aperture size over the full range of solid volume fractions has been proposed by Despois & Mortensen [16] for metal foams. Such solid foams are obtained by the so-called replication method and it was proposed to draw a parallel between the shape of pores in these foams and that of sintered (initially) spherical solid particles (more precisely, the geometrically-inversed structure of such system is considered). According to such an assumption, the dimensionless aperture size was modeled to be [16]:

$$\frac{d_o}{D_p} \cong \left(\frac{\phi_s^* - \phi_s}{3\phi_s^*}\right)^{1/2} \qquad \text{(eq. 2)}$$

Eq. 2 is plotted in Fig. 2 against experimental data (using $\phi_s^* = 0.38$) and shows significant overestimation of aperture sizes. Actually, reasonable agreement is observed only for $\phi_s \approx \phi_s^*$, which is consistent with the power law behavior expected for this regime (i.e. eq. 1). This suggests that the microstructure of (replication) metal foams differs noticeably from capillary solid foams (i.e. solidified capillary foams). The quantitative description of d_o/D_p over the full range of solid volume fraction is a difficult task. Here we consider that the complete curve d_o/D_p can be constructed by joining curves corresponding to both regimes $\phi_s \ll \phi_s^*$ and $\phi_s \approx \phi_s^*$. The latter regime is described by eq. 1. In order to obtain an expression for the first regime we assume that the length d_o is given by the difference between the typical face width L on a polyhedral bubble and the length $2xr$ covered by the peripheral Plateau borders (struts) around the face (see Fig. 1(b2)): $d_o/D_p \cong L/D_p - 2xr/D_p$, where $x \approx 2/3$ [17] and $L/D_p \approx 0.55$ [18] are geometrical coefficients. For small solid contents, Plateau border width is known to vary as [9,18,19] $r/D_p \simeq c\phi_s^{1/2}$, which gives information about d_o/D_p in this regime. Actually, good agreement is found for the latter equation (with $c \simeq 0.5$) with our data within the range $0.02 \lesssim \phi_s \lesssim 0.28$. Therefore, a piecewise function can be built from this behavior combined with Eq. 1, as well as a third-order polynomial function as a joining function:

$$\begin{cases} \phi_s \leq 0.28: \ \frac{d_o}{D_p} = 0.55 - 0.685\phi_s^{1/2} \\ 0.28 \leq \phi_s \leq 0.35: \ \frac{d_o}{D_p} = -94.000\phi_s^3 + 79.847\phi_s^2 - 23.252\phi_s + 2.501 \\ \phi_s \geq 0.35: \ \frac{d_o}{D_p} = 0.66(\phi_s^* - \phi_s)^{1/2} \end{cases} \quad \text{(eq. 3)}$$

Alternatively, we propose the following expression to describe the measured aperture size over the full range of solid volume fraction: $d_0/D_p \approx [(\phi_s^* - \phi_s)(1 - \phi_s^* + \phi_s)]^{1/2} + \phi_s(3.8\phi_s - 1.48)$.

Our data for $N_o(\phi_s)$ are partial but they can be combined with expected bounds, i.e. $N_o \approx 14$ for $\phi_s \ll 1$ (Kelvin cells [19]) and $N_o \approx 6$ for $\phi_s \approx \phi_s^*$ [20]. Fig. 1e shows that $N_o(\phi_s)$ can be described by the following relation:

$$N_o(\phi_s) \approx 2\left(7 - 4\frac{\phi_s}{\phi_s^*}\right) \quad \text{(eq. 4)}$$

Results for the foam permeability are presented in Table 1 and Fig. 3b. It is shown that all the permeability values are gathered on a single curve when plotting $k_D/V_p^{2/3}$ as a function of ϕ_s, where $V_p = \pi D_p^3/6$ is the pore volume. Data are well described by an exponential function over the full

range of solid volume fraction. However this behavior is expected to evolve strongly for $\phi_s \approx \phi_s^*$ due to the particular behavior observed for parameter d_o/D_p in this range of solid volume fractions (see Fig. 2). In the following, theoretical models are compared to the measured foam permeability.

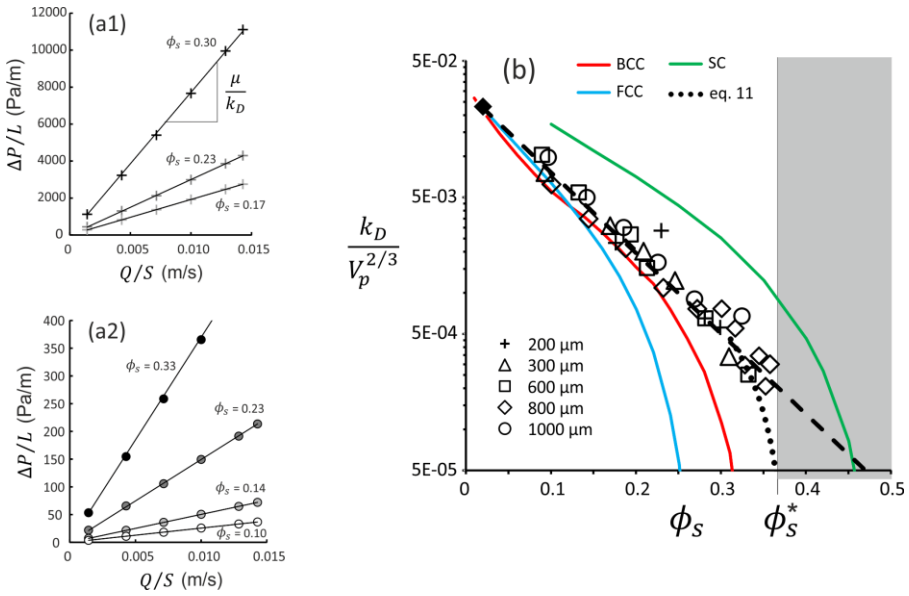

Figure 3: (a) Measured pressure gradient $\Delta P/L$ as a function of the superficial velocity Q/S. The permeability k_D is deduced from the slope of the straight line by assuming that the viscosity of the fluid is $\mu \cong 1.758\ 10^{-5}$ Pa s. Results are presented for two pore diameters, (a1) D_p = 200 µm and (a2) D_p = 1000 µm, and several solid volume fractions ϕ_s as indicated. (b) Darcy permeability k_D of the studied foam samples divided by $V_p^{2/3} = \left(\pi D_p^3/6\right)^{2/3}$. Empty symbols: experimental data for MK foam samples with different pore sizes and different solid volume fractions. Note that permeability of samples characterized by solid volume fractions $\phi_s > \phi_s^*$ (grey area) is too small to be measured with our system. Full symbol: data published by Trinh et al.[4] *for monodisperse polymer foams. The dashed line corresponds to an exponential decay: $k_D/V_p^{2/3} = 0.03 \times exp(-13.5\phi_s)$. The dotted curve corresponds to eq. 11. Continuous curves show the theoretical values for several structures: red – BCC, blue – FCC, green – SC.*

Table 1

D_p (mm)	ϕ_s	k_D (m^2)	Coef. R^2	$\overline{Re}$
0.20	0.18	5.99 10^{-11}	0.9999	0.1
0.20	0.23	7.35 10^{-11}	1.0000	0.1
0.20	0.28	1.69 10^{-11}	0.9992	0.1
0.25	0.30	2.33 10^{-11}	0.9996	0.1
0.31	0.09	4.60 10^{-10}	1.0000	0.2
0.31	0.17	1.89 10^{-10}	0.9999	0.2
0.31	0.21	1.23 10^{-10}	1.0000	0.2
0.31	0.25	7.53 10^{-11}	0.9999	0.2
0.31	0.31	2.10 10^{-11}	0.9990	0.2

0.67	0.09	$2.92\ 10^{-09}$	0.9982	0.3
0.67	0.13	$1.55\ 10^{-09}$	1.0000	0.3
0.67	0.19	$7.66\ 10^{-10}$	0.9997	0.3
0.67	0.21	$4.37\ 10^{-10}$	0.9994	0.3
0.65	0.28	$1.75\ 10^{-10}$	0.9999	0.3
0.65	0.33	$6.75\ 10^{-11}$	0.9981	0.3
0.86	0.10	$2.94\ 10^{-09}$	0.9991	0.4
0.86	0.14	$1.65\ 10^{-09}$	0.9996	0.4
0.86	0.19	$1.01\ 10^{-09}$	0.9999	0.4
0.86	0.23	$5.18\ 10^{-10}$	1.0000	0.4
0.86	0.27	$3.64\ 10^{-10}$	0.9999	0.4
0.87	0.30	$3.69\ 10^{-10}$	0.9997	0.5
0.85	0.32	$2.54\ 10^{-10}$	0.9999	0.4
0.85	0.33	$1.37\ 10^{-10}$	0.9998	0.4
0.85	0.35	$1.60\ 10^{-10}$	0.9999	0.4
0.85	0.35	$9.60\ 10^{-11}$	0.9992	0.4
0.86	0.36	$1.44\ 10^{-10}$	0.9997	0.4
1.06	0.10	$6.99\ 10^{-09}$	1.0000	0.6
1.06	0.14	$3.56\ 10^{-09}$	1.0000	0.6
1.06	0.19	$2.15\ 10^{-09}$	0.9998	0.6
1.06	0.23	$1.20\ 10^{-09}$	0.9998	0.6
1.06	0.27	$6.48\ 10^{-10}$	0.9998	0.6
1.06	0.33	$4.87\ 10^{-10}$	0.9995	0.6

The Carman-Kozeny model for permeability of porous media is based on the specific surface area A_s which is defined as the ratio of pore surface area in contact with the flowing fluid over the total volume of the porous material [21,22]. Then the permeability writes:

$$k_D = \frac{(1-\phi_s)^3}{C_K A_s^2} \quad \text{(eq. 5)}$$

C_K is the Kozeny constant and it is expected to be obtained by comparison with experimental data. For example, $C_K \approx 5$ for packings of solid spheres [23]. A_s can be estimated for $\phi_S \ll 1$, where most of the surface area is due to the slender struts, of thickness $r \sim D_p \phi_s^{1/2}$ (see Fig. 1(b2)), forming the solid foam skeleton: $A_s \sim r D_p / D_p^3$, or equivalently $D_p A_s \sim \phi_s^{1/2}$. In this regime, the fluid permeability is therefore expected to vary as $k \sim D_p^2 / \phi_s$. In order to go further, the parameter A_s is now determined from numerical simulations. Such an approach has been shown to be useful to describe the drainage liquid flow through bubbles in liquid foams [9,24,25]. A_s values have been determined by using the Surface Evolver software and the values are shown in Fig. 4a as a function of ϕ_s, as well as the corresponding permeability values against experimental data. Note that the constant C_K can be fitted in order to describe the data within the range $\phi_S \lesssim 0.1$, but significant deviations are observed for $\phi_s > 0.1$. Actually, the predicted slope $|dk/d\phi_s|$ is too low as compared to experimental data, which can be understood by the small amount (small surface area) of solid

involved in the progressive closing of the apertures compared to the strong viscous dissipation occurring in those areas.

More specific analytical models have been proposed to estimate the permeability of open-cell foams. Those models are based on various pore-scale geometric assumptions (representative unit cell) depending on the considered range of pore volume fraction. Two basic pore-scale geometries can be found in literature: struts network (see [26,27] for example) or pores connected by apertures (see for example [16,28–30]). The former are expected to be relevant for high porosity values, where foam structure can be described, indeed, as a network of slender struts. Here we compare our data with the models proposed by Yang et al. [26] and Woudberg & Du Plessis [27] which were found to compare satisfactorily with available experimental data. As shown in Fig. 4b, such models fail to predict the measured foam permeability by almost one order of magnitude, except at very high pore volume fraction. This suggests that the assumed pore-scale geometry does not describe correctly the microstructure of solid foams over the full range of solid volume fraction. More precisely, the expected strong effect of narrow apertures is not accounted for.

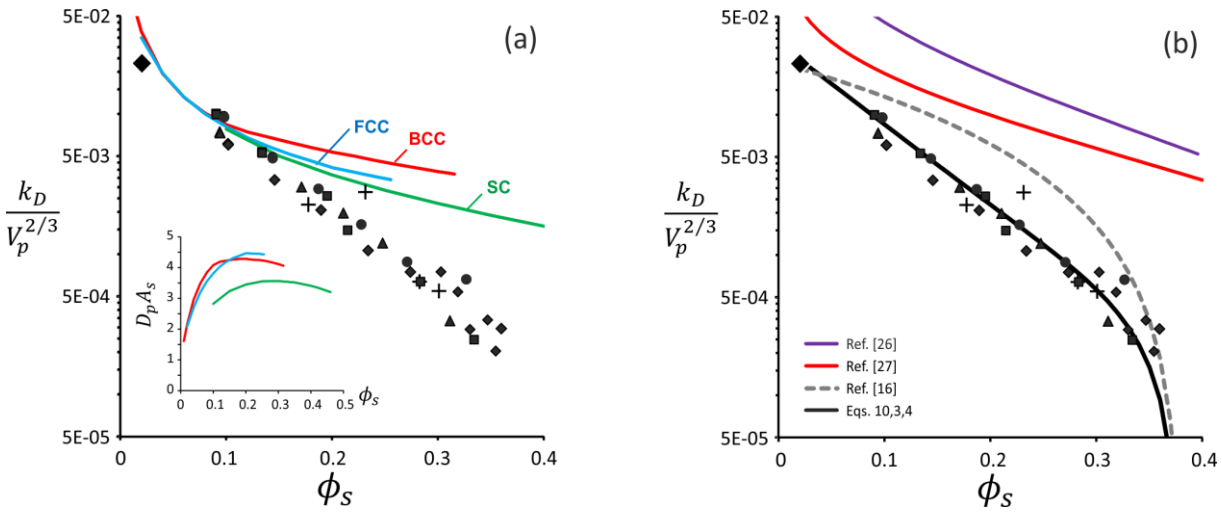

Figure 4: Foam permeability (divided by $V_p^{2/3}$) as a function of solid volume fraction. Empty symbols correspond to data already shown in Fig. 3b. Full symbol: data published by Trinh et al.[4] *for monodisperse polymer foams. (a) Values predicted by the Kozeny-Carman model (eq. 5) for three foam crystals: red – BCC, blue – FCC, green – SC. Permeability values are calculated from the specific surface area A_s determined for the three structures (see the inset). Values for the Kozeny constant C_K used in eq. 6 are the following: 10 for BCC, 11 for FCC et 20 for SC. (b) Comparison of experimental data with different models: Woudberg & Du Plessis* [27]*, Yang et al.* [26]*, Despois & Mortensen* [16]*, and eqs 10,3,4.*

The opposite approach is to consider solely the effect of apertures. This was proposed initially by Despois & Mortensen [16] and it was successfully used recently to predict the permeability in model Kelvin foam [30]. It is based on the assumption that the pressure-flow rate relation for fluid flowing through one circular aperture of diameter d_o is $q = d_o^3 \Delta p / 24\mu$, where Δp is the pressure difference across the aperture [31]. By averaging the local flow rates passing through the pores and by using eq. 2 to estimate the aperture size, the authors have proposed the following expression for the foam permeability:

$$\frac{k_D}{V_p^{2/3}} = \frac{(1-\phi_s)}{\pi(4\pi/3)^{2/3}} \left(\frac{\phi_s^* - \phi_s}{3\phi_s^*} \right)^{3/2} \quad \text{(eq. 6)}$$

Eq. 6 is plotted in Fig. 4b by assuming $\phi_s^* = 0.38$, showing poor agreement except for $\phi_s \approx 0.02$ and for $\phi_s \gtrsim 0.3$. We stress that eq. 6 assumes apertures size given by eq. 2 and that the latter was found to overestimate the measured aperture sizes. In order to fully decouple the effect of aperture size from the intrinsic ability of the model to predict foam permeability, now we consider the case of ideal foam structures for which aperture size is known (see FCC, BCC and SC curves in Fig. 2). A representative periodic foam structure is considered as enclosed in a box of cross-section area a^2 (perpendicular to the direction of the macroscopic pressure gradient) and thickness h (see Fig. 5). The Darcy permeability writes:

$$k_D = \mu \frac{Qh}{a^2 \Delta P} \quad \text{(eq. 7)}$$

where the macroscopic volume flow rate Q passing through the cross-section is related to the volume flow rates q_i exchanged with neighbor pores through apertures i: $Q = \sum_i q_i$, and ΔP is the pressure difference across the thickness h. By assuming that the flow of the fluid through each aperture of size $d_{o,i}$ within the foam structure is given by $q_i = d_{o,i}^3 \Delta P_i / 24\mu$ [31], the theoretical permeability writes [28]:

$$k_D = \mu \frac{h}{a^2 \Delta P} \sum_{i=1}^{N} q_i = \frac{1}{24} \frac{h}{a^2} \sum_{i=1}^{N} d_{o,i}^3 \frac{\Delta P_i}{\Delta P} \quad \text{(eq. 8)}$$

Note that the ratio $\Delta P_i / \Delta P$ also writes $\Delta z_i / h$, where Δz_i is the distance between centers of the two pores connected by the aperture i, measured along the direction of the macroscopic pressure gradient. As an example, the Kelvin structure presented in Fig. 5 shows 2 square faces (1 full and 4

quarters) with $\Delta P_i/\Delta P$ = 1 and 4 full hexagonal faces with $\Delta P_i/\Delta P$ = ½. Fig. 2 shows d_o/D_p as a function of ϕ_s for three foam structures: FCC (Face-Centered Cubic), BCC (Body-Centered Cubic) and SC (Simple Cubic). Foam permeability is therefore calculated by eq. 8 using results given in Fig. 2 for d_0/D_p (curves FCC, BCC and SC). Comparison with experimental data is presented in Fig. 3. The theoretical curves describe reasonably the overall decrease measured for $k/V_p^{2/3}$ as a function of ϕ_s, although none of them describes quantitatively the full set of data. More precisely, the FCC curve underestimates the data for $\phi_s \gtrsim 0.15$, the BCC curve underestimates the data for $\phi_s \gtrsim 0.3$ and the SC curve overestimates the data over the full range of solid volume fractions. This highlights issues associated to the description of the random foam structure with ideal foam crystals.

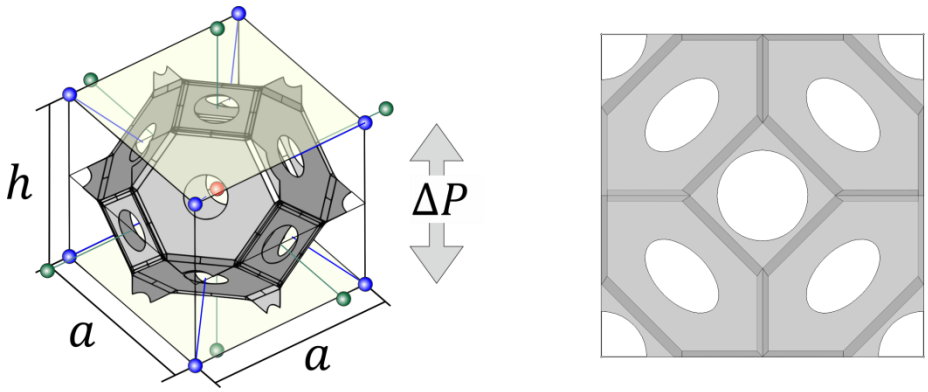

Figure 5: Sketch of a periodic foam structure (Kelvin cells). Left: The macroscopic pressure gradient corresponds to a pressure difference equal to ΔP across the cell thickness h. Centers of the neighbor pores are shown by color spheres: blue spheres are connected to the central pore (red sphere) by hexagonal faces and green spheres by square faces. Right: view from above of the same structure, i.e. it is a square of length side a. Fluid passing through such a foam structure in the direction perpendicular to cross-section a^2 has to flow through the apertures shown in the figure.

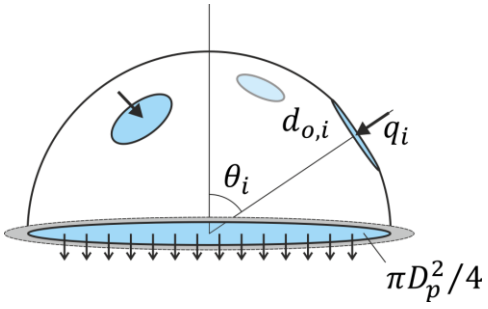

Figure 6: Mean pore of diameter D_p representing the whole foam structure (all the pore configurations). Apertures of size d_o connect the pore to N_o neighbors with witch fluid flow rates q_i are exchanged. The fluid flow rate passing through the middle cross-section of the pore is equal to the sum of the flow rates crossing the $N_o/2$ apertures located above. The angle θ_i measured the position of those apertures.

In order to overcome issues related to foam crystals, now we turn to a mean pore configuration: The permeability is estimated by assuming that pores are randomly distributed with coordination number N_o, i.e. each pore is directly connected to N_o pores through apertures characterized by a single value d_o. We consider the reference area $A = \pi D_p^2/4(1-\phi_s)$ as the middle cross-section (perpendicular to the direction of the macroscopic pressure gradient ∇P) of a spherical pore (see Fig. 6). Fluid flow passing through A is coming at flow rate $q_i = d_o^3 \Delta P_i / 24\mu$ from each one of the $N_o/2$ neighbor pores located above A, so:

$$k_D \approx \frac{\mu \sum_{i=1}^{N_o/2} q_i}{A(\Delta P/D_p)} \approx \frac{D_p}{24A}\frac{N_o}{2} d_o^3 \langle \frac{\Delta P_i}{\Delta P} \rangle \quad \text{(eq. 9)}$$

$\langle \Delta P_i \rangle / \Delta P = \langle cos\theta \rangle$ where the azimuthal angle θ is used to measure the position of the neighbor pores centers with respect to the reference pore along the direction of the macroscopic pressure gradient: $\langle cos\theta \rangle = \int_0^{\pi/2} cos\theta sin\theta d\theta = 1/2$. Therefore, the dimensionless permeability writes:

$$\frac{k_D}{V_p^{2/3}} \cong 0.02 \times (1-\phi_s) N_o \left(\frac{d_o}{D_p}\right)^3 \quad \text{(eq. 10)}$$

The case corresponding to $\phi_s \approx \phi_s^*$ can be estimated easily: the number of apertures per pore is $N_o \approx 6$ [20] and the aperture size is expected to be given by $d_o/D_p \cong 0.66(\phi_s^* - \phi_s)^{0.5}$ (see Fig. 2). Therefore eq. 10 becomes:

$$\frac{k_D(\phi_s \approx \phi_s^*)}{V_p^{2/3}} \cong 0.035 \times (1-\phi_s^*)(\phi_s^* - \phi_s)^{3/2} \quad \text{(eq. 11)}$$

Comparison with permeability data (see Fig. 3b) provides the fitted value $\phi_s^* \approx 0.38 \pm 0.02$, which is consistent with the theoretical value corresponding to packings of monodisperse spherical bubbles, i.e. 0.36 [32]. Note that predicted values are almost three times smaller than those given by eq. 6 although the power law behavior is identical.

Using eqs 10, 3 and 4 allows for the permeability to be estimated over the full range of solid volume fraction. The corresponding values are plotted in Fig. 4b and show good agreement with experimental data. Actually, as the measured exponential behavior is reasonably described by the *apertures model* (i.e. eq. 10 or eq. 6) using the measured relationship between aperture size and

solid fraction, it suggests that the observed exponential decay mainly reflects the evolution of aperture size with solid volume fraction.

This good agreement should not obscure the fact that several assumptions have been made to derive equation 10. The main issue concerns the averaging procedure for the positions of apertures around the reference plane. Moreover, a mean aperture size has been used whereas real apertures distribution should have been accounted for. In addition, the assumption of small aperture through pore faces is not fully justified for foams with small solid contents. Further investigation could help to understand how those effects interplay in the global permeability behavior.

4. Conclusion

Darcy permeability has been measured for open-cell foams with monodisperse pore diameter ranging from 200 to 1000 µm and solid volume fraction ranging from 0.1 to 0.38. The dimensionless permeability showed an exponential decay as a function of solid volume fraction, except for solid fractions close to packing volume fraction of monodisperse spheres. Existing models do not capture this exponential decay and actually they predict permeability values significantly larger than the measured values. Moreover, previously measured permeability for replication metal foams is also significantly larger than our data, suggesting that the microstructure of those metal foams differs from solid foams resulting from hardening of liquid capillary foams. The so-called *apertures model*, which is based on the assumption that most of the viscous dissipation occurs within the aperture areas that connect the pores, was found to be appropriate to reproduce the exponential behavior as soon as the measured apertures sizes is accounted for, which suggests that the exponential behavior mainly reflects the evolution of aperture size with solid volume fraction.

Acknowledgments

The authors thank P. Aimedieu (at Navier Laboratory) for technical support with the X-ray tomography. This work has benefited from French government Grant managed by the Agence Nationale de la Recherche [Grant number ANR-13-RMNP-0003-01].

Data availability

The raw/processed data required to reproduce these findings can be provided on request.

References

[1] S.Y. Kim, J.W. Paek, B.H. Kang, Flow and heat transfer correlations for porous fin in a plate-fin heat exchanger, Journal of Heat Transfer. 122 (2000) 572–578. doi:10.1115/1.1287170.

[2] Z. Zhang, J.L. Provis, A. Reid, H. Wang, Geopolymer foam concrete: An emerging material for sustainable construction, Construction and Building Materials. 56 (2014) 113–127. doi:10.1016/j.conbuildmat.2014.01.081.

[3] A. Jung, H. Natter, S. Diebels, E. Lach, R. Hempelmann, Nanonickel coated aluminum foam for enhanced impact energy absorption, Advanced Engineering Materials. 13 (2011) 23–28. doi:10.1002/adem.201000190.

[4] V.H. Trinh, V. Langlois, J. Guilleminot, C. Perrot, Y. Khidas, O. Pitois, Tuning membrane content of sound absorbing cellular foams: Fabrication, experimental evidence and multiscale numerical simulations, Materials and Design. 162 (2019) 345–361. doi:10.1016/j.matdes.2018.11.023.

[5] J.F. Allard, N. Atalla, Propagation of Sound in Porous Media: Modelling Sound Absorbing Materials, John Wiley and Sons, 2009. doi:10.1002/9780470747339.

[6] D. Edouard, M. Lacroix, C.P. Huu, F. Luck, Pressure drop modeling on SOLID foam: State-of-the art correlation, Chemical Engineering Journal. 144 (2008) 299–311. doi:10.1016/j.cej.2008.06.007.

[7] P. Kumar, F. Topin, State-of-the-Art of Pressure Drop in Open-Cell Porous Foams: Review of Experiments and Correlations, Journal of Fluids Engineering. 139 (2017) 111401. doi:10.1115/1.4037034.

[8] A. Kaddami, O. Pitois, A physical approach towards controlling the microstructure of metakaolin-based geopolymer foams, Cement and Concrete Research. 124 (2019) 105807. doi:10.13140/RG.2.2.30318.87367.

[9] I. Cantat, S. Cohen-Addad, F. Elias, F. Graner, R. Höhler, O. Pitois, F. Rouyer, Foams: Structure and Dynamics, Oxford University Press, Oxford, 2013.

[10] F.G. Gandolfo, H.L. Rosano, Interbubble Gas Diffusion and the Stability of Foams, Journal of Colloid and Interface Science. 194 (1997) 31–36. doi:10.1006/jcis.1997.5067.

[11] C.T. Rueden, J. Schindelin, M.C. Hiner, B.E. DeZonia, A.E. Walter, E.T. Arena, K.W. Eliceiri, ImageJ2: ImageJ for the next generation of scientific image data, BMC Bioinformatics. 18 (2017) 529. doi:10.1186/s12859-017-1934-z.

[12] D. Legland, I. Arganda-Carreras, P. Andrey, MorphoLibJ: integrated library and plugins for mathematical morphology with ImageJ, Bioinformatics. 32 (2016) 3532–3534. doi:10.1093/bioinformatics/btw413.

[13] N. Otsu, A Threshold Selection Method from Gray-Level Histograms, IEEE Transactions on Systems, Man, and Cybernetics. 9 (1979) 62–66. doi:10.1109/TSMC.1979.4310076.

[14] J.P. Bonnet, F. Topin, L. Tadrist, Flow laws in metal foams: Compressibility and pore size effects, Transport in Porous Media. 73 (2008) 233–254. doi:10.1007/s11242-007-9169-5.

[15] D. Whyte, R. Murtagh, D. Weaire, S. Hutzler, Applications and extensions of the Z-cone model for the energy of a foam, Colloids and Surfaces A: Physicochemical and Engineering Aspects. 473 (2015) 115–122. doi:10.1016/j.colsurfa.2014.12.041.

[16] J.F. Despois, A. Mortensen, Permeability of open-pore microcellular materials, Acta Materialia. 53 (2005) 1381–1388. doi:10.1016/j.actamat.2004.11.031.

[17] E. Lorenceau, N. Louvet, F. Rouyer, O. Pitois, Permeability of aqueous foams, European Physical Journal E. 28 (2009) 293–304. doi:10.1140/epje/i2008-10411-7.

[18] L.J. Gibson, M.F. Ashby, Cellular Solids: Structure and Properties, Cambridge University Press, Cambridge, 1997.

[19] D.L. Weaire, S. Hutzler, The Physics of Foams, Oxford University Press, Oxford, 2001.

[20] P.M. Chaikin, A. Donev, W. Man, F.H. Stillinger, S. Torquato, Some Observations on the Random Packing of Hard Ellipsoids, Ind. Eng. Chem. Res. 45 (2006) 6960–6965. doi:10.1021/ie060032g.

[21] J. Kozeny, Ueber kapillare Leitung des Wassers im Boden, Sitzungsber Akad. Wiss. 136 (1927) 271–306.

[22] P.C. Carman, Fluid flow through granular beds, Trans. Instn Chem. Engrs. 15 (1937) 150–166. doi:10.1016/S0263-8762(97)80003-2.

[23] F.A.L. Dullien, Porous media : fluid transport and pore structure, Academic Press, 1991.

[24] O. Pitois, E. Lorenceau, N. Louvet, F. Rouyer, Specific surface area model for foam permeability, Langmuir. 25 (2009) 97–100. doi:10.1021/la8029616.

[25] F. Rouyer, O. Pitois, E. Lorenceau, N. Louvet, Permeability of a bubble assembly: From the very dry to the wet limit, Physics of Fluids. 22 (2010) 043302. doi:10.1063/1.3364038.

[26] X. Yang, T.J. Lu, T. Kim, An analytical model for permeability of isotropic porous media, Physics Letters, Section A: General, Atomic and Solid State Physics. 378 (2014) 2308–2311. doi:10.1016/j.physleta.2014.06.002.

[27] S. Woudberg, J.P. Du Plessis, An analytical Ergun-type equation for porous foams, Chemical Engineering Science. 148 (2016) 44–54. doi:10.1016/j.ces.2016.03.013.

[28] A.J. Otaru, A.R. Kennedy, The permeability of virtual macroporous structures generated by sphere packing models: Comparison with analytical models, Scripta Materialia. 124 (2016) 30–33. doi:10.1016/j.scriptamat.2016.06.037.

[29] L. Weber, D. Ingram, S. Guardia, A. Athanasiou-Ioannou, A. Mortensen, Fluid flow through replicated microcellular materials in the Darcy-Forchheimer regime, Acta Materialia. 126 (2017) 280–293. doi:10.1016/j.actamat.2016.12.067.

[30] V. Langlois, V.H. Trinh, C. Lusso, C. Perrot, X. Chateau, Y. Khidas, O. Pitois, Permeability of solid foam: Effect of pore connections, Physical Review E. 97 (2018) 053111. doi:10.1103/PhysRevE.97.053111.

[31] R.A. Sampson, On Stokes's Current Function, Philosophical Transactions of the Royal Society A: Mathematical, Physical and Engineering Sciences. 182 (1891) 449–518. doi:10.1098/rsta.1891.0012.

[32] S. Torquato, T.M. Truskett, P.G. Debenedetti, Is Random Close Packing of Spheres Well Defined?, Physical Review Letters. 84 (2000) 2064–2067.